Solar RRL

WILEY VCH

Solar RRL

RESEARCH ARTICLE OPEN ACCESS

Nonvolatile Solid Additive with a Simple Structure for Nonfullerene Organic Solar Cells

Do Hui Kim[1] | Dong Chan Lee[1] | Sujung Park[1] | Jiwoo Yeop[2] | Sung-Yeon Jang[2] | Jin Young Kim[2] | Shinuk Cho[1]

[1]Department of Semiconductor Physics and Engineering & EHSRC, University of Ulsan, Ulsan, Republic of Korea | [2]Department of Energy Engineering & School of Energy and Chemical Engineering, Ulsan National Institute of Science and Technology (UNIST), Ulsan, Republic of Korea

Correspondence: Shinuk Cho (sucho@ulsan.ac.kr)

Received: 25 March 2025 | **Revised:** 19 April 2025 | **Accepted:** 24 April 2025

Funding: Research Fund of University of, Grant/Award Number: Ulsan (2025−0327)

Keywords: nonvolatile | organic solar cells | solid additive

ABSTRACT

In organic solar cells (OSCs), precise control over the bulk heterojunction (BHJ) morphology is critical for optimizing device performance. A widely adopted strategy for regulating BHJ morphology involves the incorporation of small amounts of additives. However, employing volatile solid additives necessitates precise volatilization control, which remains challenging. While nonvolatile solid additives with high boiling points have been explored, most exhibit large and structurally complex architectures, raising concerns regarding their role in OSCs and their potential impact on charge transport. Thus, a nonvolatile solid additive with both a high boiling point and a simple molecular structure is highly desirable. In this study, 4-bromobiphenyl (BBP), a nonvolatile solid additive with a high boiling point and a simple chemical structure, was incorporated into OSCs to modulate BHJ morphology. The addition of BBP enhanced donor–acceptor miscibility, suppressed excessive aggregation, and promoted a uniform morphology with improved crystallinity. Consequently, the power conversion efficiency significantly increased to 18.11%, surpassing that of OSCs incorporating volatile solid additives while also enhancing long-term stability. This work provides a promising strategy for achieving stable BHJ morphology and improving OSC performance through nonvolatile solid additives.

1 | Introduction

Organic solar cells (OSCs) have rapidly advanced, achieving high power conversion efficiency (PCE) since the advent of nonfullerene acceptors (NFAs), which offer advantages such as a suitable absorption range and easily tunable energy levels [1–3]. To commercialize OSCs, numerous efforts have been made to enhance their PCE, including the development of novel NFAs such as Y6 derivatives, modifications to the charge transport layer, and morphological optimization of the photoactive layer [4–9]. Among these approaches, optimizing the morphology of the photoactive layer in bulk heterojunction (BHJ) structures is particularly critical for further enhancing OSC performance, as this layer plays a pivotal role in light absorption and charge generation [10–12].

The application of additives is one of the most common techniques for optimizing the morphology of BHJ, facilitating controlled phase separation and the formation of a well-defined interpenetrating network. The majority of OSCs based on Y6 derivatives have primarily relied on small amounts of solvent additives, such as 1-chloronaphthalene (CN) and 1,8-diiodooctane (DIO), to regulate the morphology of the BHJ by leveraging their selective solubility for donor and acceptor materials [13–15]. However, it is essential to recognize that NFAs exhibit an exceptional sensitivity to minute amounts of solvent additives due to their inherent strong aggregation property [16, 17]. The typical volume of solvent additives used is only a few microliters per 10 mL of BHJ solvent. It is practically very challenging to achieve fine control over this aspect. Excessive use of solvent

additives induces extreme phase separation, leading to a rapid decline in OSC performance.

Recently, the adoption of solid additives as an alternative to solvent additives has been increasing, owing to their ease of handling and good miscibility with NFAs. Solid additives enable precise control over phase separation and domain purity while minimizing process-induced variability. Moreover, their incorporation enhances reproducibility and long-term stability by mitigating inconsistencies inherent to solvent additive processing. Compared to solvent additives, which generally have relatively high boiling points (Bp), most of the solid additives reported to date exhibit lower boiling points and predominantly volatile characteristics [18, 19].

Volatile solid additives appear to regulate BHJ morphology through a mechanism distinct from that of solvent additives. It has been reported that solid additives prevent excessive NFA aggregation by modulating their miscibility with photoactive materials, intermolecular interactions, and the volatilization process [20–23]. Bao et al. utilized high-crystallinity dithieno[3,2-*b*:2′, 3′-*d*]thiophene (DDT), which exhibits good miscibility with Y6, as a volatile solid additive in conjunction with a CN solvent additive [24]. During the thermal annealing process, DDT volatilized, allowing PM6 to occupy the remaining space and suppress the excessive self-assembly of NFAs. Similarly, the volatile solid additive 2-hydroxy-4-methoxybenzophenone (2-HM) functions as a regulator of BHJ morphology by interacting with the functional groups of Y6 [21]. Its volatilization induces the assembly of PM6 and Y6 into a more ordered face-on orientation with enhanced π–π stacking, leading to improved charge transport properties and reduced charge recombination.

Although volatile solid additives have demonstrated significant advantages in regulating BHJ morphology, their practical application still faces certain limitations. In particular, the dependence of morphology on the volatilization process and incomplete volatilization can lead to morphological instability. The solid additive 1-chloro-4-iodobenzene (CIB), which has a high boiling point of 227°C, formed a BHJ film with a more uniform fibrillar morphology and enhanced crystallinity compared to 1,4-diiodobenzene (DIB), which has a lower boiling point of 174°C [25]. This observation suggests that excessively rapid volatilization of solid additives may hinder the optimal formation of BHJ morphology, ultimately leading to poor exciton separation and inefficiency in charge transport.

These findings highlight the necessity of nonvolatile solid additives as an alternative approach to overcoming the limitations associated with volatile counterparts. However, as mentioned earlier, most reported solid additives still exhibit volatile characteristics. Although several nonvolatile solid additives have been explored, they typically possess large and structurally complex molecular architectures [26, 27]. The role of such large and complex solid additives remains debatable, whether they should be considered merely as morphological regulators or treated similarly to ternary solar cell components. Therefore, we have identified the need for nonvolatile solid additives with high boiling points and structurally simple compositions to achieve both morphological stability and practical applicability.

In this study, we applied 4-bromobiphenyl (BBP), a nonvolatile solid additive with a simple chemical structure and a high boiling point of 310°C, to PM6:L8-BO-based OSCs. To investigate the effect of the nonvolatile nature of BBP on device performance, a comparative analysis was performed on OSCs incorporating CN as a representative solvent additive and 2-HM as a volatile solid additive with a low boiling point of 150°C. The addition of BBP improved the miscibility of PM6 and L8-BO more effectively than CN and 2-HM. Due to its nonvolatile property, BBP remained in the active layer of PM6:L8-BO even after thermal annealing, preserving its ideal morphology. This morphological enhancement contributed to increased crystallinity in PM6:L8-BO films, leading to higher and more balanced electron and hole mobilities. This reduction in trap-assisted recombination and trap density resulted in lower energy loss. Consequently, the OSC with BBP as an additive exhibited an outstanding PCE of 18.11%, surpassing those of OSCs incorporating the solvent additive CN and the rapidly volatilizing solid additive 2-HM. This work provides a promising strategy for optimizing stable BHJ morphology through the incorporation of a nonvolatile solid additive to achieve high-efficiency OSCs.

2 | Results and Discussion

Figure 1a presents the chemical structures of the CN, 2-HM, and BBP additives used in this study. The devices were fabricated with the conventional structure of indium tin oxide (ITO)/Br-2EPSe/active layer/PDINN/Ag, as illustrated in Figure 1b. Br-2EPSe is a self-assembled monolayer (SAM) material used to modify the surface of ITO. Detailed information is available in other literature [28]. The current density–voltage (J–V) characteristics of the devices with different additives are shown in Figure 1c, and the corresponding detailed device parameters are summarized in Table 1. The devices incorporating CN and 2-HM were fabricated following previously reported methods, while the device with BBP was optimized, as shown in Figure S1 [15, 21, 29].

The PM6:L8-BO-based device without any additives exhibited a PCE of 15.01%, with a short-circuit current density (J_{SC}) of 25.41 mA cm^{-2}, an open-circuit voltage (V_{OC}) of 0.846 V, and a fill factor (FF) of 69.81%. The device incorporating CN as a solvent additive demonstrated an increased J_{SC} of 26.39 mA cm^{-2}, an almost identical V_{OC} of 0.851 V, and an enhanced FF of 74.13%, resulting in a higher PCE of 16.65% compared to the additive-free device. Similarly, the device with a volatile solid additive 2-HM exhibited a comparable PCE of 16.73% to that of the CN-based device, with a J_{SC} of 27.51 mA cm^{-2}, a V_{OC} of 0.811 V, and an FF of 74.96%. Despite the superior crystallinity improvement due to the rapid volatilization of 2-HM, no enhancement in V_{OC} was observed.

In contrast, the device incorporating the nonvolatile solid additive BBP, which has a high boiling point of 310°C, achieved a significantly higher PCE of 18.11% without any deterioration in V_{OC}, yielding a J_{SC} of 27.78 mA cm^{-2}, a V_{OC} of 0.852 V, and an FF of 76.52%. The statistical histograms of the PCE of devices with and without additives are presented in Figure 1d, demonstrating that the BBP-based device achieved the highest average efficiency. To confirm the universal applicability of

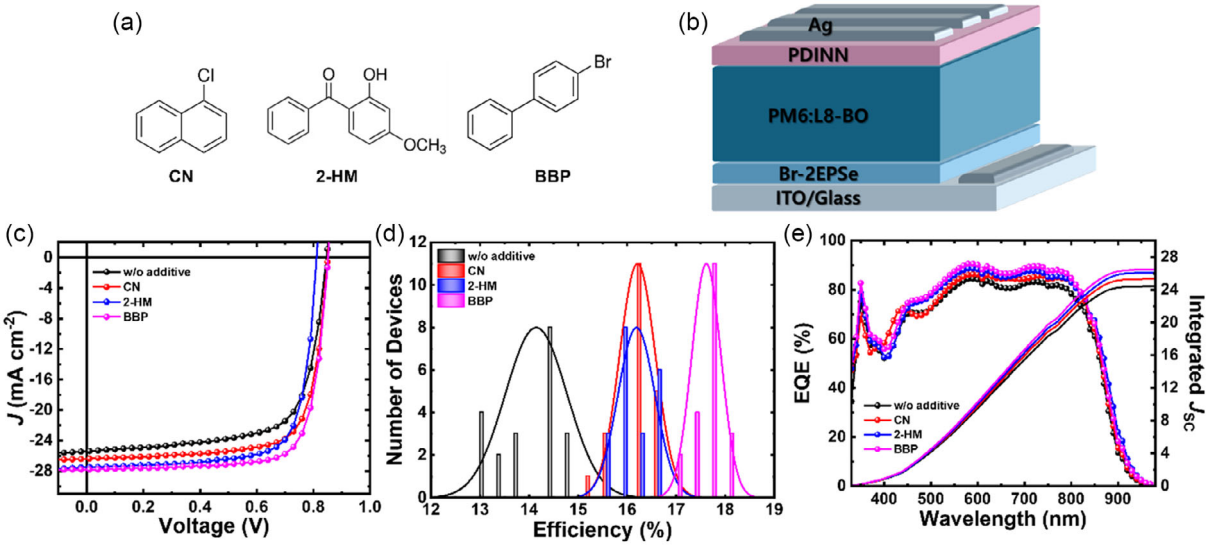

FIGURE 1 | (a) Chemical structures of the solvent additive CN, volatile solid additive 2-HM, and nonvolatile solid additive BBP. (b) Device structure: ITO/Br-2EPSe/active layer/PDINN/Ag. (c) *J*–*V* characteristics of PM6:L8-BO-based devices fabricated without additive and with CN, 2-HM, and BBP additives. (d) Statistical histogram of device PCEs. (e) EQE spectra and corresponding integrated J_{SC} values of the devices. 2-HM = 2-hydroxy-4-methoxybenzophenone; BBP = 4-bromobiphenyl; CN = 1-chloronaphthalene; EQE = external quantum efficiency; *J*–*V* = density–voltage.

TABLE 1 | Photovoltaic parameters of PM6:L8-BO-based devices fabricated without additives and with CN, 2-HM, or BBP. Average values were obtained from 20 devices.

Additive	J_{SC} [mA cm^{-2}]	V_{OC} [V]	FF	PCE [%]
w/o additive	25.41 (24.04 ± 1.339)	0.846 (0.842 ± 0.014)	69.81 (69.98 ± 2.454)	15.01 (14.14 ± 0.617)
CN	26.39 (25.82 ± 0.672)	0.851 (0.847 ± 0.004)	74.13 (74.07 ± 0.415)	16.65 (16.21 ± 0.359)
2-HM	27.51 (26.90 ± 0.291)	0.811 (0.807 ± 0.012)	74.96 (74.53 ± 0.963)	16.73 (16.19 ± 0.369)
BBP	27.78 (27.29 ± 0.544)	0.852 (0.851 ± 0.005)	76.52 (75.78 ± 0.462)	18.11 (17.61 ± 0.291)

BBP, it was further tested in various photoactive layers. As shown in Figure S2 and Table S2, BBP resulted in similar performance improvements in PM6:Y6 and PM6:ITIC-4F-based devices. Figure 1e presents the corresponding external quantum efficiency (EQE) spectra and integrated J_{SC} values, which are in good agreement with the J_{SC} values obtained from *J*–*V* measurements.

Fourier transform infrared (FTIR) measurements were conducted to characterize the volatility of the additives. Figure S3 shows the FTIR spectra of PM6:L8-BO blend films with and without annealing treatment, using CN and 2-HM additives, respectively. The PM6:L8-BO blend film with CN exhibited a characteristic FTIR absorption peak at 765 cm^{-1}, which disappeared after annealing treatment [22]. The characteristic absorption peaks of 2-HM at 633, 700, and 1027 cm^{-1} were clearly observed before annealing treatment in the PM6:L8-BO blend film with 2-HM, but these peaks vanished after annealing treatment [21]. These results indicate that both CN and 2-HM additives exhibit volatile properties. In contrast, as shown in Figure 2a, the PM6:L8-BO blend film with BBP displayed a clear characteristic FTIR absorption peak at 756 cm^{-1}, which remained evident even after annealing treatment, indicating that BBP is nonvolatile and persists after annealing.

Figure 2b,c shows the absorption spectra of neat PM6 and L8-BO films with different additives. The intensity ratio of the 0–0 peak to the 0–1 peak in PM6 films varied depending on the additive used. Notably, the PM6 film with BBP exhibited the highest 0–0/0–1 peak intensity ratio, indicating significantly enhanced molecular ordering. In contrast, L8-BO films showed greater sensitivity to additives compared to PM6 films, with BBP again providing the most substantial improvement in molecular stacking relative to CN and 2-HM. To further confirm these observations, grazing-incidence wide-angle X-ray scattering (GIWAXS) measurements were performed, as presented in Figure S4 and S5. The PM6 films with additives showed improved face-on crystallinity compared to the additive-free film. Morphological changes induced by additives were even more prominent in L8-BO films. Specifically, the molecular packing behavior of L8-BO varied significantly with the type of additive used. As shown in Figure S5, the L8-BO film with the solvent additive CN exhibited a distinct, enhanced single π–π stacking peak in the out-of-plane (OOP) direction. In contrast, the L8-BO films containing solid additives (2-HM and BBP) exhibited multiple diffraction peaks over a broad range (1–2 Å^{-1}) in the OOP direction, as well as multiple lamellar peaks appearing within the range of 0.3–0.5 Å^{-1} in the in-plane (IP) direction. These results clearly indicate that NFAs are more sensitive to additives than polymer donors, leading to distinctly different molecular stacking structures.

The miscibility between PM6 and L8-BO, depending on the additives, was estimated using the Flory–Huggins interaction

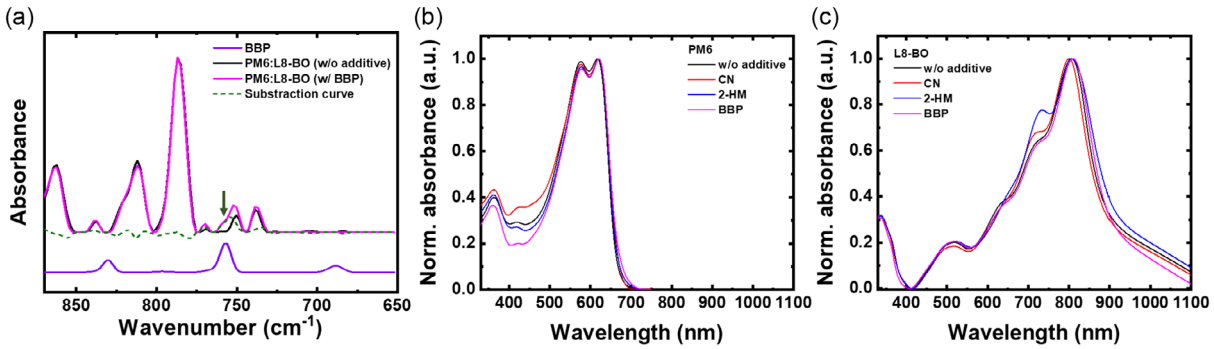

FIGURE 2 | (a) FTIR spectra of pure BBP and PM6:L8-BO blend films with and without BBP after thermal annealing at 130°C for 10 min. Normalized absorption spectra of (b) PM6 and (c) L8-BO films prepared without additives and with CN, 2-HM, or BBP. 2-HM = 2-hydroxy-4-methoxybenzophenone; BBP = 4-bromobiphenyl; CN = 1-chloronaphthalene; FTIR = Fourier transform infrared.

parameter (χ), calculated as $\chi \propto ({\gamma_1}^{1/2} - {\gamma_2}^{1/2})^2$, where γ represents the surface energy of the neat PM6 and L8-BO films with and without additives [29, 30]. Figure S6 presents the contact angles of water and ethylene glycol on PM6 and L8-BO films with different additives. The calculated χ values for PM6:L8-BO blends were 0.0627K (without additive), 0.1679K (with CN), 0.1491K (with 2-HM), and 0.0994K (with BBP) (Table S3). A lower χ value indicates higher miscibility between PM6 and L8-BO, which helps suppress excessive phase separation and promotes the formation of a favorable interpenetrating network in the BHJ. These results suggest that the solid additive BBP enhances the miscible interaction between PM6 and L8-BO more effectively than CN and 2-HM.

To investigate the intermolecular interactions between BBP and PM6, as well as BBP and L8-BO, FTIR measurements were conducted on PM6 and L8-BO films with and without BBP [18, 31, 32]. As shown in Figure S7, the PM6 film exhibited a characteristic carbonyl peak at 1649.0 cm^{-1}. Upon the addition of BBP, this peak slightly shifted to 1648.3 cm^{-1}, indicating intermolecular interactions between PM6 and BBP. Similarly, the characteristic FTIR peaks of L8-BO also changed upon BBP addition. The pristine L8-BO film exhibited peaks corresponding to alkyl chain vibrations (~1423 cm^{-1}), C═C stretching (~1533 cm^{-1}), and cyano group vibrations (~2216 cm^{-1}). These peaks shifted to 1423.2, 1531.7, and 2215.4 cm^{-1}, respectively, in the presence of BBP. These results suggest that BBP forms strong intermolecular interactions with both PM6 and L8-BO, leading to optimized morphology and enhanced crystallinity of the active layer.

Figure 3 presents the atomic force microscopy (AFM) images of PM6:L8-BO blend films with and without additives. The blend film without additives exhibited the smoothest surface morphology, with a root-mean-square (RMS) roughness of 0.947 nm, whereas the blend films with CN, 2-HM, and BBP showed increased roughness values of 1.366, 1.746, and 0.954 nm, respectively. This suggests that the addition of additives facilitated the formation of more pronounced nanofibrillar structures, as confirmed by the AFM phase images in Figure S8. The PM6:L8-BO blend film with CN formed larger fibrillar structures compared to those with 2-HM and BBP, which was attributed to the relatively low miscibility between PM6 and L8-BO in the presence of CN. Interestingly, although 2-HM exhibited higher miscibility than CN, it resulted in a nonuniform morphology. In contrast, BBP, which demonstrated the highest miscibility, formed a more uniform and well-defined nanofibrillar texture. This optimized active morphology appears to have contributed to the improvement of J_{SC} and FF in the device.

To further investigate the molecular orientation and crystallization of PM6:L8-BO blend films with and without additives, GIWAXS measurements were performed. Figure 4 presents the GIWAXS images and corresponding line-cut profiles of PM6:L8-BO blend films without additives and with CN, 2-HM, and BBP. The corresponding fitting results are listed in Table S4. All blend films, both with and without additives, exhibited a face-on orientation, showing π–π stacking peaks at 1.712, 1.727, 1.725, and 1.733 $Å^{-1}$ in the OOP direction for blend films without additives and with CN, 2-HM, and BBP, respectively. These results indicate that the π–π stacking distance decreased upon the introduction of additives, with the most pronounced decrease from 3.670 to 3.626 Å observed in the blend film with BBP. Interestingly, despite the high volatility of 2-HM, it exhibited poorer π–π stacking than CN. The crystal coherence lengths (L_C) in the OOP direction were calculated using the Scherrer equation [33, 34–35]. As shown in Table S4, the estimated L_C values were 14.92, 19.17, 17.67, and 20.20 Å, indicating that the PM6:L8-BO blend films with additives formed a more compact molecular packing than those without additives. Among them, the BBP additive demonstrated the highest capability for enhancing molecular packing. This improvement in the crystallinity and molecular packing properties of the PM6:L8-BO blend film with BBP appears to have significantly impacted charge transport.

Figure 5a and S10 present the space charge limited current (SCLC) measurements used to examine the electron and hole transport properties in electron-only and hole-only devices. The estimated electron (μ_e) and hole mobilities (μ_h) of the PM6:L8-BO blend films with and without additives are listed in Table S5. The device without additives exhibited low μ_e and μ_h values of 7.38×10^{-4} and 4.90×10^{-4} $cm^2\ V^{-1}\ s^{-1}$, respectively. Notably, the μ_h of the device without additives was significantly lower than μ_e, disrupting the balance of μ_e and μ_h ($\mu_e/\mu_h = 1.506$) and leading to a remarkably low FF. Meanwhile, devices with additives exhibited increased μ_e and μ_h values, with the improvement in μ_h being more pronounced. Among them, the device with BBP demonstrated the highest μ_e of

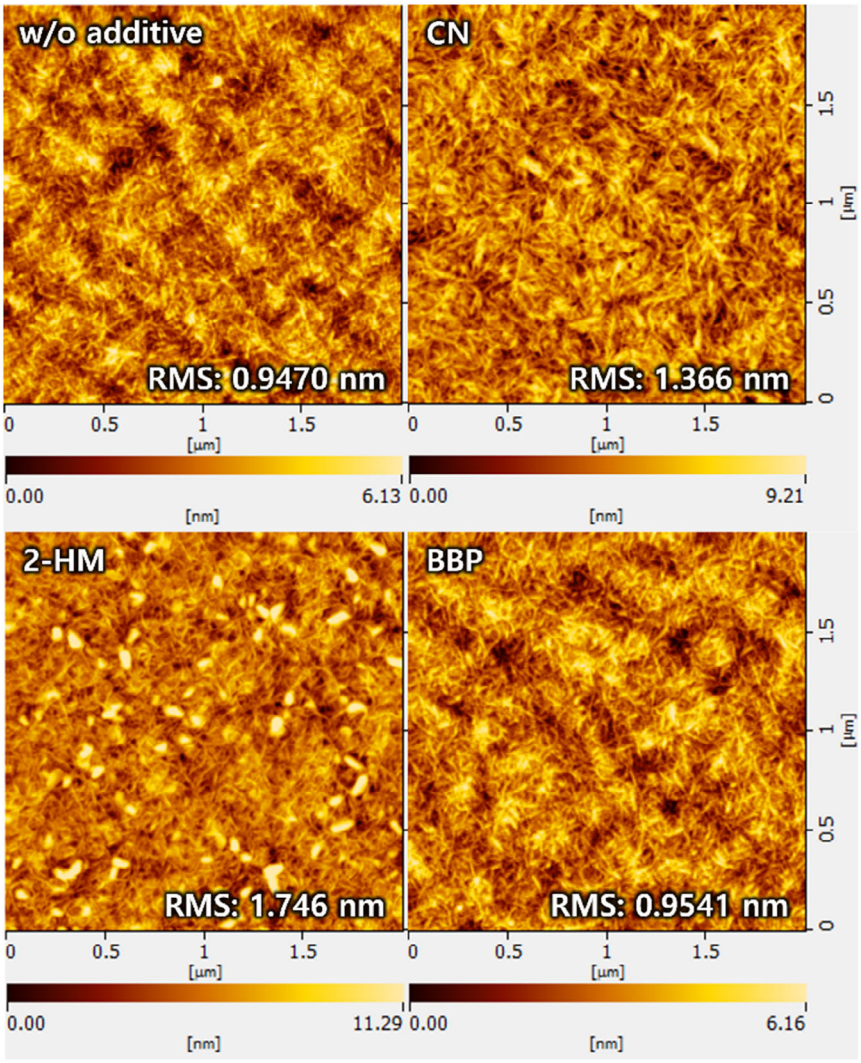

FIGURE 3 | AFM topographic images of the PM6:L8-BO blend films prepared without additive and with CN, 2-HM, or BBP additives. 2-HM = 2-hydroxy-4-methoxybenzophenone; AFM = atomic force microscopy; BBP = 4-bromobiphenyl; CN = 1-chloronaphthalene.

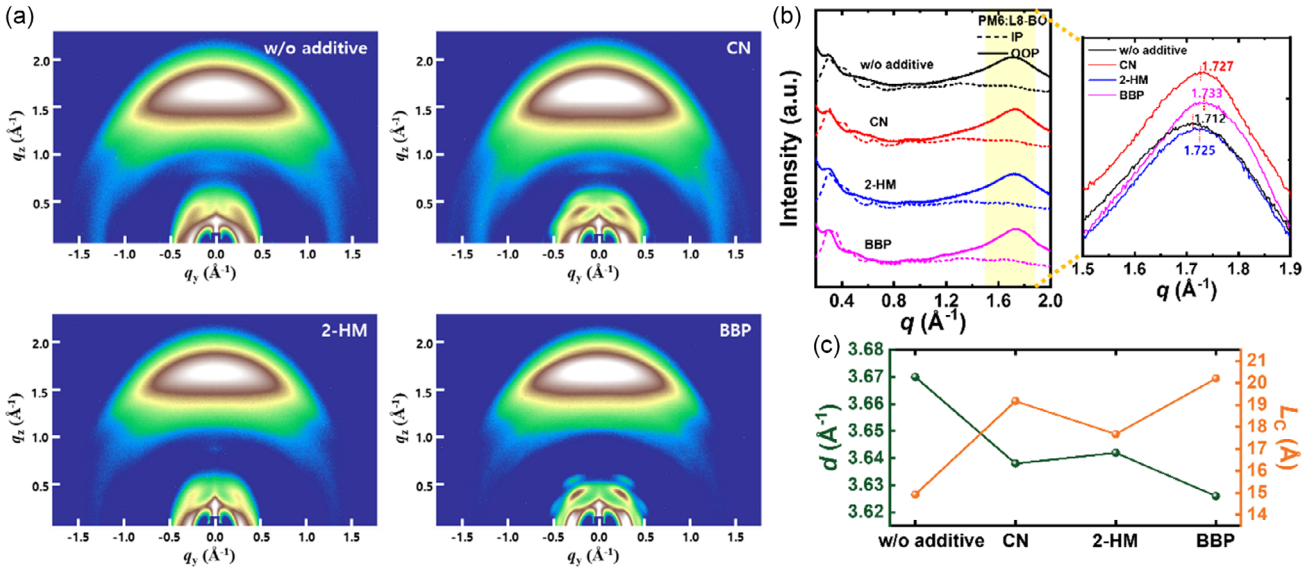

FIGURE 4 | (a) GIWAXS diffraction patterns, (b) corresponding line-cut profiles in the in-plane (IP) and out-of-plane (OOP) directions, and (c) comparison of π–π stacking distances (d) and crystal coherence lengths (L_C) in the OOP direction for PM6:L8-BO blend films prepared without additives and with CN, 2-HM, or BBP. 2-HM = 2-hydroxy-4-methoxybenzophenone; BBP = 4-bromobiphenyl; GIWAXS =grazing-incidence wide-angle X-ray scattering.

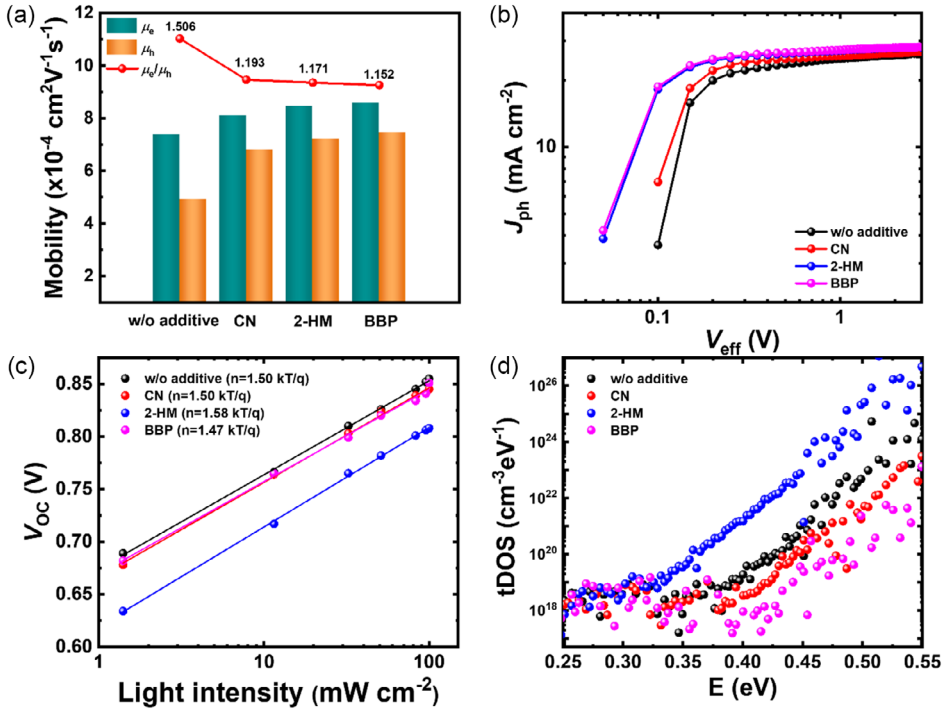

FIGURE 5 | (a) Ratio of electron to hole mobilities (μ_e/μ_h), (b) photocurrent density (J_{ph}) versus effective voltage (V_{eff}) curves, (c) light-intensity dependence of V_{OC}, and (d) trap density of states distributions for PM6:L8-BO devices prepared without additives and with CN, 2-HM, or BBP. 2-HM = 2-hydroxy-4-methoxybenzophenone; BBP = 4-bromobiphenyl; CN = 1-chloronaphthalene.

8.58×10^{-4} cm^2 V^{-1} s^{-1} and μ_h of 7.45×10^{-4} cm^2 V^{-1} s^{-1}, achieving a more balanced μ_e/μ_h ratio of 1.152.

Figure 5b presents the photocurrent density (J_{ph}) as a function of effective voltage (V_{eff}) for devices with and without additives. J_{ph} was calculated using the equation $J_{ph} = J_L - J_D$, where J_L is the current density under illumination and J_D is the current density in the dark. V_{eff} was determined as $V_0 - V$, where V_0 represents the voltage at $J_{ph} = 0$ and V is the applied bias voltage [31, 32]. The maximum exciton generation rate (G_{max}) is defined by the equation $J_{sat} = qLG_{max}$, where q is the elementary charge, L is the thickness of the photoactive layer, and J_{sat} is the saturated photocurrent density (when $V_{eff} > 2$V). Notably, devices with the solid additives 2-HM and BBP exhibited a significant increase in G_{max} values, rising from 1.64×10^{28} to 1.76×10^{28} m^{-3} s^{-1} (Table S6). The exciton dissociation probability (P_{diss}) was obtained by dividing J_{ph} under short-circuit conditions by J_{sat}, while the charge collection probability (P_{coll}) was estimated by dividing J_{MPP} at the maximum power point by J_{sat} [36–39]. Devices without additives exhibited the lowest P_{diss} and P_{coll} values of 94.4% and 79.0%, respectively, both of which increased upon the addition of additives. The device with CN showed a P_{diss} of 95.4% and a P_{coll} of 83.9%, while the device with 2-HM exhibited a P_{diss} of 96.1% and a P_{coll} of 83.9%. Meanwhile, the device with BBP, a solid additive that facilitates the formation of a uniform and homogeneous phase, achieved the highest P_{diss} of 96.7% and P_{coll} of 85.7%, indicating that the generated excitons were effectively separated and collected, leading to an enhancement in J_{SC} and FF.

The light intensity (I) dependence of J_{SC} and V_{OC} was examined to gain insight into the impact of additives on charge recombination. Figure S11 presents the relationship between J_{SC} and I for devices with and without additives, expressed as $J_{SC} \propto I^{\alpha}$ [40, 41]. The fitted slopes (α) were 1.01, 1.02, 1.02, and 1.01 for devices without additives and with CN, 2-HM, and BBP, respectively. The α values of all devices were close to unity, indicating that bimolecular recombination is negligible regardless of the presence and type of additives. On the other hand, the light intensity dependence of V_{OC} exhibited a different trend, as shown in Figure 5c. The relationship between V_{OC} and I is expressed as $V_{OC} \propto (nkT/q)$ ln$I$, where k is the Boltzmann constant, T is the absolute temperature in Kelvin, and q is the elementary charge. The slope (n) values for devices without additives and with CN, 2-HM, and BBP were 1.50 kT/q, 1.50 kT/q, 1.58 kT/q, and 1.47 kT/q, respectively [42, 43]. These results indicate that BBP effectively suppressed trap-assisted recombination, whereas 2-HM induced more severe trap-assisted recombination compared to the device without additives.

Figure 5d and S12 show the trap density of states for devices with and without additives, determined by frequency-dependent capacitance measurements. The device with the nonvolatile solid additive BBP exhibited the lowest trap density of states in both shallow and deep trap levels. In contrast, the device with the volatile solid additive 2-HM had the highest trap density of states, which was even more severe than that of the device without additives across both shallow and deep trap states. These results indicate that 2-HM increased the trap density at both shallow and deep trap levels, leading to a degradation in V_{OC}.

To verify whether there are additional causes for the low V_{OC} in the device using 2-HM, an energy loss analysis was conducted as shown in Figure 6 and Table 2. The total energy loss (ΔE_{loss}) values were 0.583, 0.582, 0.602, and 0.573 eV for devices without additives and with CN, 2-HM, and BBP, respectively. The device

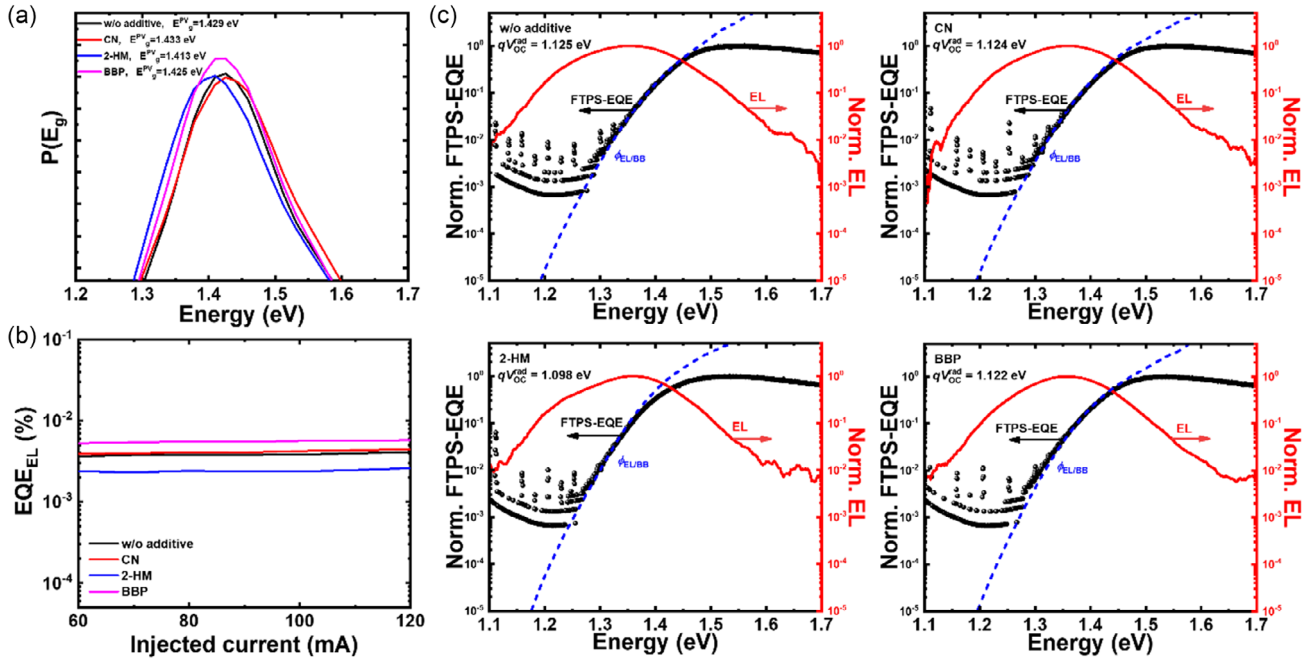

FIGURE 6 | (a) Bandgap distributions, (b) electroluminescence external quantum efficiency (EQE_{EL}), and (c) Fourier-transform photocurrent spectroscopy (FTPS) and electroluminescence (EL) spectra of PM6:L8-BO-based devices fabricated without additives and with CN, 2-HM, or BBP. 2-HM = 2-hydroxy-4-methoxybenzophenone; BBP = 4-bromobiphenyl; CN = 1-chloronaphthalene.

TABLE 2 | Detailed energy loss (E_{loss}) parameters for PM6:L8-BO devices fabricated without additives and with CN, 2-HM, or BBP. All values are expressed in eV.

Additive	E_g	qV^{SQ}_{OC}	qV^{rad}_{OC}	qV_{OC}	ΔE_1	ΔE_2	ΔE_3 (EL/BB)	ΔE_3 (EQE_{EL})	ΔE_{loss}
w/o additive	1.429	1.147	1.125	0.846	0.282	0.022	0.279	0.260	0.583
CN	1.433	1.151	1.124	0.851	0.282	0.027	0.273	0.256	0.582
2-HM	1.413	1.132	1.098	0.811	0.281	0.034	0.287	0.272	0.602
BBP	1.425	1.143	1.122	0.852	0.282	0.021	0.270	0.249	0.573

using the nonvolatile additive BBP exhibited the lowest ΔE_{loss}, whereas the device using 2-HM, which has high volatility, exhibited the highest ΔE_{loss}. This difference is primarily attributed to radiative energy loss (ΔE_2) and nonradiative energy loss (ΔE_3). The device using 2-HM had the highest ΔE_2 value of 0.034 eV and a ΔE_3 value of 0.272 eV, calculated from EQE_{EL}, indicating a more severe energy loss compared to devices without additives and with CN. In contrast, the device using BBP exhibited the lowest energy loss, with a ΔE_2 of 0.021 eV and a ΔE_3 of 0.249 eV. To further explore this phenomenon, the Urbach energy (E_U) of the device was analyzed through exponential fitting of the Fourier-transform photocurrent spectroscopy (FTPS)-EQE spectra [2, 44, 45]. As shown in Figure S13, the device with 2-HM had the highest E_U of 26.3 meV, while the device with BBP had the lowest E_U of 24.5 meV. This suggests that the rapid volatility of 2-HM increases energetic disorder, leading to a higher ΔE_2. Furthermore, insufficient regulation of crystallinity results in a larger ΔE_3, which contributes to a reduction in V_{OC}.

The storage stability was evaluated using devices stored under dark conditions in a glove box with an N_2 atmosphere. As shown in Figure 7, the efficiency of the device without additives decreased to less than 80% of its initial value after 400 h. In contrast, devices with additives retained over 80% of their initial efficiency. Among them, the device with CN exhibited the poorest long-term stability. This is attributed to residual CN due to incomplete volatilization, which, as widely reported, continuously affected the morphology of the active layer and accelerated the degradation of device stability [20, 22, 46, 47]. On the other hand, devices using 2-HM and BBP demonstrated relatively higher stability compared to the device with CN. This highlights the importance of maintaining a stable morphology in the active layer to ensure long-term device stability. Notably, the device with BBP, a nonvolatile solid additive, exhibited outstanding stability, retaining over 90% of its initial efficiency even after 400 h. This is attributed to the enhanced crystallinity of the active layer induced by BBP, which contributes to a well-ordered morphology within the active layer.

To further evaluate the thermal stability of the devices, tests were conducted under the same conditions as the storage stability measurements (ie, stored in a nitrogen atmosphere and under dark conditions), with a thermal stress of 70°C. As shown in Figure S14, the thermal stability followed a similar trend to that

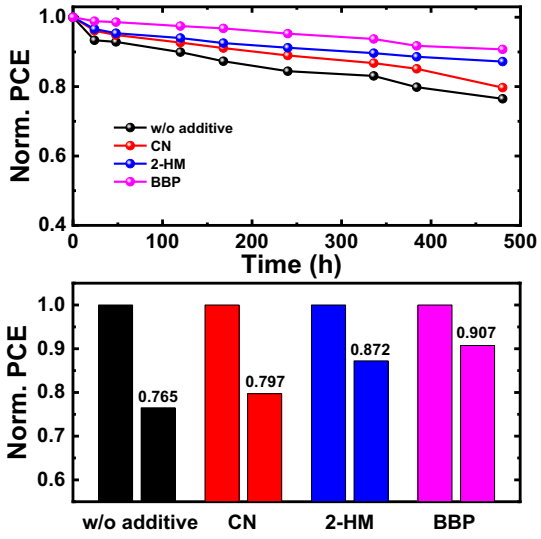

FIGURE 7 | Stability of unencapsulated PM6:L8-BO devices fabricated without additives and with CN, 2-HM, or BBP, stored under dark conditions in an N_2 atmosphere. 2-HM = 2-hydroxy-4-methoxybenzophenone; BBP = 4-bromobiphenyl; CN = 1-chloronaphthalene.

observed in the storage stability test. The device containing CN exhibited rapid degradation after 190 h, showing behavior comparable to that of the device without an additive. In contrast, devices incorporating the solid additives 2-HM and BBP exhibited significantly improved thermal stability. Notably, the device with BBP retained over 80% of its initial efficiency after 240 h, indicating the highest thermal stability among the tested devices.

3 | Conclusion

In summary, we demonstrated the beneficial effects of BBP, a nonvolatile solid additive with a simple chemical structure, into OSCs. Unlike common volatile additives, BBP remained in the active layer even after thermal annealing, ensuring superior morphological stability over extended periods. The addition of BBP significantly improved device performance, achieving a maximum PCE of 18.11%. This enhancement is attributed to the favorable miscibility between PM6 and L8-BO induced by BBP, facilitating a more uniform and distinct nanofibrillar texture, which contributed to increased J_{SC} and FF. Moreover, the improved molecular packing due to BBP resulted in increased and balanced electron and hole mobilities. Importantly, OSCs incorporating BBP significantly outperformed devices employing conventional solvent additives CN and volatile solid additives 2-HM. BBP provided good morphological stability, reduced trap density, and enhanced molecular packing. The results highlight the potential of structurally simple, nonvolatile solid additives like BBP as promising alternatives to traditional additives, offering a clear pathway toward more efficient, stable OSCs.

Acknowledgements

This work was supported by the Research Fund of University of Ulsan (2025-0327).

Data Availability Statement

The data that support the findings of this study are available from the corresponding author upon reasonable request.

References

1. C. Sun, J. Wang, F. Bi, et al., *Energy & Environmental Science* 18 (2025): 862.

2. X. Kong, N. Yang, X. Zhang, et al., *Energy & Environmental Science* 18 (2025): 386.

3. W. Feng, Y. Bai, J. Wang, et al., *Advanced Energy Materials* (2024), https://doi.org/10.1002/aenm.202404062.

4. S. Zhu, S. Chen, L. Hong, et al., *Advanced Functional Materials* 34 (2024): 2410786.

5. C. Zhang, Y. Shi, J. Tao, et al., *Advanced Energy Materials* 15 (2024): 2403806.

6. Y. Wang, K. Sun, C. Li, et al., *Advanced Materials* 36 (2024): 2411957.

7. W. Wang, S. Zhang, T. Zhang, et al., *Advanced Energy Materials* (2024), https://doi.org/10.1002/aenm.202404482.

8. L. Hu, J. Quan, J. Li, et al., *Advanced Materials* 36 (2024): 2413232.

9. S. Gao, R. Peng, Y. Qiu, et al., *Advanced Functional Materials* 35 (2024): 2418223.

10. C. Song, S. Lou, S. Deng, et al., *Solar RRL* 7 (2023): 2300567.

11. H. Yang, C. Song, T. Xia, et al., *Journal of Materials Chemistry C* 9 (2021): 12819.

12. C. Song, H. Yang, F. Liu, L. Ye, and G. J. Cheng, *Advanced Materials Interfaces* 7 (2020): 2001021.

13. X. Chen, M. Chen, J. Liang, et al., *Advanced Materials* 36 (2024): 2313074.

14. S. Liu, J. Wang, S. Wen, et al., *Advanced Materials* 36 (2024): 2312959.

15. X. Deng, B. Huang, Y. Fang, et al., *Advanced Functional Materials* 34 (2024): 2315476.

16. S. Karuthedath, Y. Firdaus, A. D. Scaccabarozzi, et al., *Small Structures* 3 (2022): 2100199.

17. O. Alqahtani, J. Lv, T. Xu, et al., *Small* 18 (2022): 2202411.

18. N. Wei, H. Lu, Y. Wei, et al., *Energy & Environmental Science* 18 (2025): 2298.

19. Y. Cheng, H. Li, X. Zhang, et al., *Advanced Functional Materials* 35 (2025): 2415468.

20. J. Xie, J. Deng, Y. Pei, et al., *Advanced Functional Materials* 34 (2024): 2402281.

21. X. Yang, B. Li, X. Zhang, et al., *Advanced Materials* 35 (2023): 2301604.

22. L. Zhong, S.-H. Kang, J. Oh, et al., *Advanced Functional Materials* 32 (2022): 2201080.

23. R. Yu, H. Yao, Y. Xu, et al., *Advanced Functional Materials* 31 (2021): 2010535.

24. S. Bao, H. Yang, H. Fan, et al., *Advanced Materials* 33 (2021): 2105301.

25. L. Kong, Z. Zhang, N. Zhao, et al., *Advanced Energy Materials* 13 (2023): 2300763.

26. L. Liu, Y. Kan, K. Gao, et al., *Advanced Materials* 32 (2020): 1907604.

27. K.-E. Hung, Y.-S. Lin, Y.-J. Xue, et al., *Advanced Energy Materials* 12 (2022): 2103702.

28. A. Ulla, K. H. Park, Y. Lee, et al., *Advanced Functional Materials* 32 (2022): 2208793.

29. J. Lv, H. Tang, J. Huang, et al., *Energy & Environmental Science* 14 (2021): 3044.

30. X. Wang, C. Feng, P. Liu, Z. He, and Y. Cao, *Small* 18 (2022): 2107106.

31. X. Li, Y. Wu, H. Yang, et al., *Advanced Functional Materials* (2025), https://doi.org/10.1002/adfm.202503986.

32. F. Wang, J. Yu, S. Wang, et al., *Chemical Engineering Journal* 485 (2024): 150081.

33. J. Wang, Y. Wang, P. Bi, et al., *Advanced Materials* 35 (2023): 2301583.

34. S. Wu, W. Feng, L. Meng, et al., *Nano Energy* 103 (2022): 107801.

35. G. M. Su, T. V. Pho, N. D. Eisenmenger, et al., *Journal of Materials Chemistry A* 2 (2014): 1781.

36. L. Tanguy, P. Malhotra, S. P. Singh, G. Brisard, G. D. Sharma, and P. D. Harvey, *ACS Applied Materials & Interfaces* 11 (2019): 28078.

37. J.-D. Chen, C. Cui, Y.-Q. Li, et al., *Advanced Materials* 27 (2015): 1035.

38. H. Guan, Q. Liao, T. Huang, et al., *ACS Applied Materials & Interfaces* 15 (2023): 25774.

39. F. T. A. Wibowo, N. V. Krishna, S. Sinaga, S. Lee, W. T. Hadmojo, Y. R. Do, and S. -Y. Jang, *Cell Reports Physical Science* 2 (2021): 100517.

40. L. Lu, W. Chen, T. Xu, and L. Yu, *Nature Communications* 6 (2015): 7327.

41. S. R. Cowan, A. Roy, and A. J. Heeger, *Physical Review B* 82 (2010): 245207.

42. Y. Zeng, D. Li, H. Wu, et al., *Advanced Functional Materials* 32 (2022): 2110743.

43. K. Jiang, G. Zhang, G. Yang, et al., *Advanced Energy Materials* 8 (2018): 1701370.

44. X. Wu, Y. Gong, X. Li, et al., *Angewandte Chemie International Edition* 64 (2024): e202416016.

45. C. Kaiser, O. J. Sandberg, N. Zarrabi, W. Li, P. Meredith, and A. Armin, *Nature Communications* 12 (2021): 3988.

46. L. Ye, Y. Cai, C. Li, et al., *Energy & Environmental Science* 13 (2020): 5117.

47. A. Tournebize, A. Rivaton, H. Peisert, and T. Chassé, *Journal of Physical Chemistry C* 119 (2015): 9142.

Supporting Information

Additional supporting information can be found online in the Supporting Information section.